Research Article

Surfactant−Polymer Complexation and Competition on Drug Nanocrystal Surfaces Control Crystallinity

Lucas Attia, Dien Nguyen, Devashish Gokhale, Talia Zheng, and Patrick S. Doyle*

Cite This: ACS Appl. Mater. Interfaces 2024, 16, 34409−34418

Read Online

ACCESS | Metrics & More | Article Recommendations | Supporting Information

ABSTRACT: Nanosizing drug crystals has emerged as a successful approach to enabling oral bioavailability, as increasing drug crystal surface area improves dissolution kinetics and effective solubility. Recently, bottom-up methods have been developed to directly assemble nanosized crystals by leveraging polymer and surfactant excipients during crystallization to control crystal size, morphology, and structure. However, while significant research has investigated how polymers and other single additives inhibit or promote crystallization in pharmaceutical systems, there is little work studying the mechanistic interactions of multiple excipients on drug crystal structure and the extent of crystallinity, which can influence formulation performance. This study explores how the structure and crystallinity of a model hydrophobic drug crystal, fenofibrate, change as a result of competitive interfacial chemisorption between common nonionic surfactants (polysorbate 80 and sorbitan monooleate) and a surface-active polymer excipient (methylcellulose). Classical molecular dynamics simulations highlight how key intermolecular interactions, including surfactant−polymer complexation and surfactant screening of the crystal surface, modify the resulting crystal structure. In parallel, experiments generating drug nanocrystals in hydrogel thin films validate that drug crystallinity increases with an increasing weight fraction of surfactant. Simulation results reveal a connection between accelerated dynamics in the bulk crystal and the experimentally measured extent of crystallinity. To our knowledge, these are the first simulations that directly characterize structural changes in a drug crystal as a result of excipient surface composition and relate the experimental extent of crystallinity to structural changes in the molecular crystal. Our approach provides a mechanistic understanding of crystallinity in nanocrystallization, which can expand the range of orally deliverable small molecule therapies.

KEYWORDS: nanoformulations, molecular dynamics, interfaces, polymers, surfactants, crystallinity
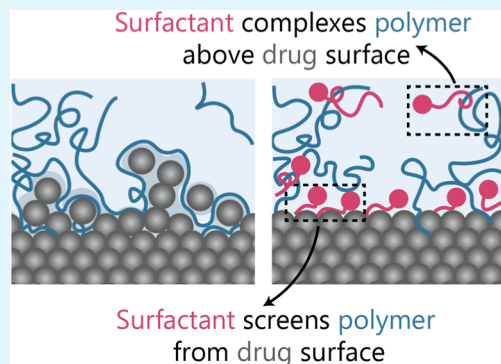
1. INTRODUCTION

The hydrophobicity of many small molecule active pharmaceutical ingredients (APIs) causes slow dissolution in the aqueous environment of the gastrointestinal tract and results in poor absorption from oral solid dosage forms.[1] Poor oral bioavailability has been a major challenge in drug development, contributing to clinical trial failures and increasing drug product costs for orally delivered therapeutics.[2] It is estimated that nearly 90% of candidate small molecules in the drug development pipeline are poorly water-soluble, motivating the development of formulations that can overcome poor solubility and slow dissolution.[3,4] In response, enabling formulations, including nanosized drug crystals and amorphous solid dispersions (ASDs), have been developed to enable oral bioavailability. Nanosized crystals exhibit improved drug dissolution kinetics and increased apparent solubility due to their increased drug surface area.[5,6] Recently, new bottom-up methods have been developed that directly assemble nanosized crystals, bypassing the difficulties of conventional top-down methods.[3] Such bottom-up methods tend to blur the boundaries between drug substance and drug product

manufacturing by including excipients in the crystallization process.[7] For example, one such bottom-up process, flash nanoprecipitation, produces polymer-coated drug nanoparticles through antisolvent precipitation in a turbulent mixing device.[8,9] Another approach developed in our research group crystallizes drug nanoparticles by encapsulating and then evaporating drug-loaded nanodroplets inside hydrogel matrices, enabling high drug-loaded formulations of hydrophobic APIs with controllable drug release.[10−15] In parallel, formulating hydrophobic drugs into ASDs has also improved the dissolution and bioavailability for many drugs.[16] ASDs exploit the ability of a polymer matrix to stabilize amorphous aggregates of drug molecules and inhibit crystallization, which promotes rapid drug release during delivery.[17] These
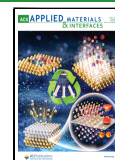
approaches can overcome poor API crystal properties since they do not require the formation of neat crystals, instead leveraging excipients like polymers and surfactants during crystallization to control crystal size, morphology, and structure, or stabilize amorphous drug aggregates.[7]

A common theme in enabling formulations is the interaction of drug surfaces with multicomponent mixtures or multiphase materials that may include polymers, surfactants, and higher-order assemblies thereof.[18] However, while some research has investigated how polymers and other single additives inhibit or promote crystallization in pharmaceutical,[19−21] mineral,[22] and chemical processes,[23] there is little work investigating the mechanistic interactions of multiple excipients on drug crystal structure and crystallinity.[24−26] These experimental studies suggest that complex interfacial interactions on growing crystal surfaces give rise to different crystallization behaviors, including the formation of amorphous drug aggregates, but limited mechanistic molecular insights can be drawn from these macro-scale crystallization experiments. Control over the extent of crystallinity in nanoformulations and ASD formulations is crucial since crystallinity can directly influence dissolution rate and bioavailability.[27,28] In parallel, molecular simulations have been used to probe fundamental atomistic interactions in pharmaceutical crystallization systems[29−33] and potential mechanisms of crystallization inhibition by polymers in ASDs.[34] However, no work has investigated how the structure of drug crystals and the extent of drug crystallinity or amorphicity change as a result of realistic compositional changes in polymer and surfactant excipients. Simulating pharmaceutical crystals with realistic excipient crystallization conditions can unlock mechanistic insights, which can inform formulation design.

Here, we explore how the extent of crystallinity of a model hydrophobic drug crystal (fenofibrate, FEN) changes as a result of competitive chemisorption between nonionic surfactants (polysorbate 80 and sorbitan monooleate) and a surface-active polymer (methylcellulose), which are commonly used excipients in the pharmaceutical industry.[35] We first develop a molecular dynamics (MD) workflow to simulate interfacial interactions on organic molecular crystals. Using this workflow, we simulate the effect of surfactant weight fraction at experimentally realistic compositions on the crystal structure and dynamics. We corroborate our simulation results using the bottom-up nanocrystallization method developed in our group[10−15] to relate the excipient composition and interfacial structure to the experimentally observed extent of crystallinity. These are the first simulations that directly characterize structural changes in a drug crystal as a result of excipient surface composition and relate experimental extent of crystallinity to molecular-level structure. Our approach provides mechanistic understanding of bottom-up crystallization and enables control over crystallinity, which can expand the range of orally deliverable small molecule therapies.

2. SIMULATION DESIGN

2.1. System Selection and Molecular Models. Molecular structures of polysorbate 80 (TW80) and sorbitan monooleate (SP80) were obtained from the automatic topology builder database.[36] Methylcellulose (MC) oligomers were constructed using Avogadro,[37] with a degree of methyl-group substitution of 2.0 and 10 monomer units, a commonly used oligomer length for MC simulations.[38] The rationale and design of the MC oligomers are further discussed in

Supporting Information, Section S1. These molecular models were used to generate GROMACS topology files using the automatic topology maker SwissParam.[39] SwissParam uses the dihedral angle term and the quadratic part of the bond and angle energy terms from the Merck molecular force field.[39] The CHARMM all-atom force field is used for simulations.[40] CHARMM is frequently used for simulating pharmaceutical systems.[41−43] This force field parametrization approach was previously validated for cellulose-derived oligomers.[38] This MD workflow is summarized in Figure S1 (Supporting Information).

The FEN polymorph form I unit cell was obtained as a CIF from the literature.[44] Using this CIF, FEN crystal slabs were prepared in Mercury (Cambridge Crystallographic Data Centre)[45] for the three dominant crystallographic surfaces of FEN: (100), (010), and (001).[29] FEN crystal slabs were designed with a constant thickness of 5 nm to sample surface interactions and crystal structure and stability far from the surface. Crystal slabs are approximately 24 nm × 24 nm × 5 nm, centered in a 24 nm × 24 nm x 30 nm simulation box. To maintain a 5 nm thickness, 5 unit cells are stacked in the (100) and (010) crystal slabs, while 3 unit cells are stacked in the (001) crystal slab. The simulation box dimensions were selected to avoid periodic artifacts from the MC oligomers, which are the longest molecules in the system with a maximum end-to-end length ≈12 nm. To anchor the FEN crystal slab in the simulation box, isotropic point position restraints with a force constant k = 1000 kJ mol^{-1} nm^{-2} were applied to every atom in the bottom unit cell layer of the slab (Section S3, Supporting Information). The triclinic FEN unit cell gives rise to nonrectangular slabs, so a Python script was written to cut the (010) and (001) slabs and fit them into a rectangular simulation box (Section S4, Supporting Information).

2.2. Simulation Setup. The ratios of excipient molecules (MC and TW80/SP80) used in the simulations were derived from experimental conditions used in our group's nano-crystallization approach (Section S5, Supporting Information). The weight fraction of surfactant ($w_{surfactant}$, defined below in eq 1) is used to directly connect the experimental conditions and the compositions used in simulations

$$w_{surfactant} = \frac{m_{surfactant}}{m_{surfactant} + m_{polymer}} \qquad (1)$$

where $m_{surfactant}$ is the mass of surfactant (TW80 or SP80) and $m_{polymer}$ is the mass of polymer (MC) in the experimental system or simulation. Simulations were designed with the following compositions: $w_{surfactant} \in \{0, 0.09, 0.16, 0.27\}$. After calculating $w_{surfactant}$, this ratio was scaled to an extensive number of MC and surfactant molecules using a constant density of 0.40 g mL^{-1} of excipients in the ~3 nm vacuum layer above the crystal surface, achieving a constant total mass of excipients across all simulations. The excipients are inserted at a reduced density to make the MC oligomer insertion computationally tractable. Within the vacuum layer, excipients were inserted in alternating layers to ensure sufficient interactions between the excipients and drug crystals to reach equilibrium on a practical simulation time scale (Section S6, Supporting Information). The full details of the compositions of the simulations are available in Table S1 (Supporting Information).

2.3. Molecular Dynamics. All simulations were performed in GROMACS 2021,[46] using a time step of 1.75 fs and a cutoff of 1.122 nm for short-range electrostatics and van der Waals

interactions. Long range electrostatics were modeled using the particle-mesh-Ewald method with a Fourier spacing of 0.12 nm. Bonds were constrained with the LINCS algorithm. The simulations sampled the *NVT* ensemble at 300 K using the velocity-rescaling thermostat with a stochastic term.[47] A 10,000-step energy minimization was performed using the steepest descent algorithm with a maximum step size of 0.01 nm and a maximum force tolerance of 10 kJ mol^{-1} nm^{-1}. Following energy minimization, an *NVT* equilibration was performed using the leapfrog algorithm for integration. The simulations ran for 19.25 ns, and the structural and energetic properties of both the excipients and the crystal reached equilibrium after ≈16 ns (Section S7, Supporting Information). To ensure only equilibrium properties were analyzed, only the final 0.36 ns were used for structural and energetic analysis. Since our simulations are computationally intensive, only select simulations were replicated to ensure reproducibility. We observe minimal differences in energetic and structural properties between replicate simulations, indicating our simulation approach is robust (Section S13, Supporting Information).

The Debye−Waller Factor (DWF, also called *B*-factor) is used to analyze thermal fluctuations in the crystal, and is defined in eqs 2 and 3 below

$$\text{DWF}_i = \frac{8\pi^2}{3}(\rho_i)^2 \tag{2}$$

$$\rho_i = \sqrt{\langle(\mathbf{r_i} - \langle\mathbf{r_i}\rangle)^2\rangle} \tag{3}$$

where $\mathbf{r}_i$ is the coordinate vector of atom i and ρ_i is the root-mean-square fluctuation (RMSF) of an atom.[48] A low DWF describes a structural moiety that is localized, while a high DWF describes a flexible moiety. For molecular crystals, higher DWF values indicate amorphization.[49] The root-mean-square deviation (rmsd) is also calculated as a deviation from the crystal lattice positions using eq 4 below

$$\text{rmsd}(t) = \left[\frac{1}{N}\sum_{i=1}^{N}\left\|\mathbf{r}_i(t) - \mathbf{r}_i^{\text{ref}}(0)\right\|^2\right]^{1/2} \tag{4}$$

where N is the number of atoms in the selection, $\mathbf{r}_i(t)$ is the coordinate vector of an atom at time t, and $\mathbf{r}_i^{\text{ref}}(0)$ is the coordinate vector of the original lattice position of an atom. The self-radial distribution function (RDF) of the FEN crystal is computed to analyze the structural order in the crystal. The self-RDF is renormalized using eqs 2 and 3

$$\tilde{g}(r) = \frac{g(r)r}{\lim\limits_{r\to l}g(r)r} \tag{5}$$

where $g(r)$ is the RDF, r is the radial distance, and l is the dimension of the box, 24 nm. This renormalization reveals structural differences on the crystal surface and ensures that $\tilde{g}(r)$ asymptotes to 1.

3. EXPERIMENTAL SECTION

3.1. Materials. MC (viscosity: 15 cP, $M_w \approx 14{,}000$ g mol^{-1}), FEN, anisole, Tween 80 (polysorbate 80), and Span 80 (sorbitan monooleate) were purchased from Sigma-Aldrich and used without further modification.

3.2. Nanoemulsion Synthesis. The nanoemulsions prepared for bottom-up nanocrystallization are made up of a continuous aqueous phase and a dispersed oil phase. The continuous phase was a 4 wt %

MC aqueous solution. The dispersed phase was a saturated FEN-in-anisole solution. The saturated solution was prepared by adding bulk FEN crystals into anisole until additional crystals settled and could not be further dissolved. To synthesize the nanoemulsions, a pre-emulsion was prepared by mixing and vortexing varying amounts of the continuous phase, dispersed phase, and surfactant (Tween 80 or Span 80) in a 50 mL conical Falcon tube. The nanoemulsion compositions for different surfactant and surfactant mass are summarized in Table S2 (Supporting Information). The masses of the continuous and dispersed phases were fixed at 3.0 and 0.3 g, respectively. The pre-emulsion mixture was then placed in a 24 mm diameter horn ultrasonicator (Cole-Parmer) and sonicated at 30% amplitude for 30 min at a frequency of 20 kHz. The ultrasonicator was kept at 10 °C with a circulating cooling water bath.

3.3. Preparation of Nanocrystalline Thin Films. A 75 mm × 25 mm × 1 mm microscope slide (plain glass, VWR VistaVision) was used as a substrate for the thin film. The mass of nanoemulsion on each slide was fixed at 2.0 g. After nanoemulsion was transferred via pipet onto the slide, the slide was quickly moved to a 70 °C oven and dried for 24 h to evaporate the anisole and water. Once dried, the thin film was removed from the slide and stored in a closed vial at room temperature for further characterization and analysis.

3.4. Differential Scanning Calorimetry. Thermal analysis of the thin films was performed using a differential scanning calorimeter (TA Instruments DSC 2500). The sample chamber environment was kept inert using a nitrogen purge at a flow rate of 50 mL min^{-1}. Approximately 5 mg of ground sample was loaded into Tzero pans and lids. The sample was equilibrated at 10 °C, and then the temperature was ramped up to 150 °C at a ramp rate of 10 °C min^{-1}. Then, an isothermal step at 150 °C was held for 5 min.

3.5. Scanning Electron Microscopy. The solid-state morphology of the dried thin films was characterized using a high-resolution scanning electron microscope (Zeiss HRSEM). Samples were prepared on SEM specimen stubs with carbon tape and sputter-coated with 5 nm of gold prior to imaging to improve contrast. An accelerating voltage of 3 kV and a probe current of 120 pA were used.

3.6. X-ray Diffraction. The crystalline structures of the drugs loaded in the thin films were characterized via X-ray diffraction (XRD) using an in-reflection mode (Phillips PANalytical X'Pert Pro MPD). The instrument was operated at a constant voltage of 45 kV and a constant current of 20 mA. For preparing the samples, the dried thin films were ground with a mortar and pestle into a fine powder suitable for XRD analysis. The powder sample was placed on a silicon crystal zero diffraction plate. The diffraction angle 2θ was swept from 4 to 40° by 0.0167° at a scanning rate of 2° min^{-1}.

3.7. Calculation of Extent of Crystallinity. The crystallinity of the FEN nanocrystals embedded in the thin film nanocomposites was characterized using a previously developed protocol.[13,50] A correlation of fusion enthalpy (ΔH_{fusion}, J g^{-1}) and melting temperature (T_{mp}, °C) of FEN was extracted from Dwyer et al.[50] This approach assumes that each DSC curve represents a distribution of melting points (T_{mp}), from which a degree of crystallinity of FEN nanocrystals (Γ_{FEN}) can be estimated by taking the ratio of the crystalline FEN mass ($m_{\text{FEN, crystalline}}$) to the total FEN mass in a sample (m_{FEN}), as shown below in eq 6. Finally, m_{FEN} is estimated using the predicted drug loading of FEN in the dried nanocomposite thin film via mass balance

$$\Gamma_{\text{FEN}} = \frac{m_{\text{FEN,crystalline}}}{m_{\text{FEN}}} \times 100 \tag{6}$$

To calculate $m_{\text{FEN, crystalline}}$, a DSC melting experiment (described above) is performed on a nanocomposite thin film. Then, a spline is fit on the resulting thermogram and integrated using eq 7

$$m_{\text{FEN,crystalline}} = \int_{-\infty}^{\infty} \frac{\dot{H}m_{\text{sample}}}{\dot{T}\Delta H_{\text{fusion}}}\,\mathrm{d}T_{\text{mp}} \tag{7}$$

where $\dot{H}$ is the spline fit of the specific heat flow (W g^{-1}), m_{sample} is the mass of nanocomposite thin film (g), and $\dot{T}$ is the heating rate (°C s^{-1}).
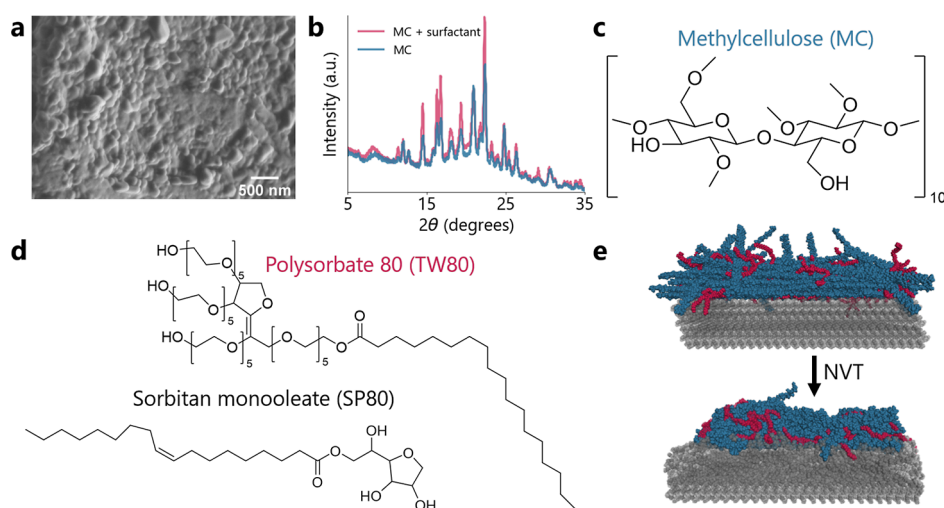
Figure 1. We study surfactant-dependent drug crystallinity using MD simulations and experiments. (a) Representative SEM micrograph of a polymer film containing bottom-up FEN nanocrystals. Scale bar represents 500 nm. (b) XRD scattering pattern of composite film with (red) and without (blue) surfactant. (c) Molecular structure of the MC oligomer model used in simulations. (d) Molecular structures of TW80 and SP80, the surfactants used in this work. (e) Overview of modeling approach, wherein MC (blue) and surfactant (red) self-assemble on FEN (gray) crystal surfaces, and the resulting excipient and drug structures reveal the molecular mechanisms driving surfactant-dependent crystallinity.
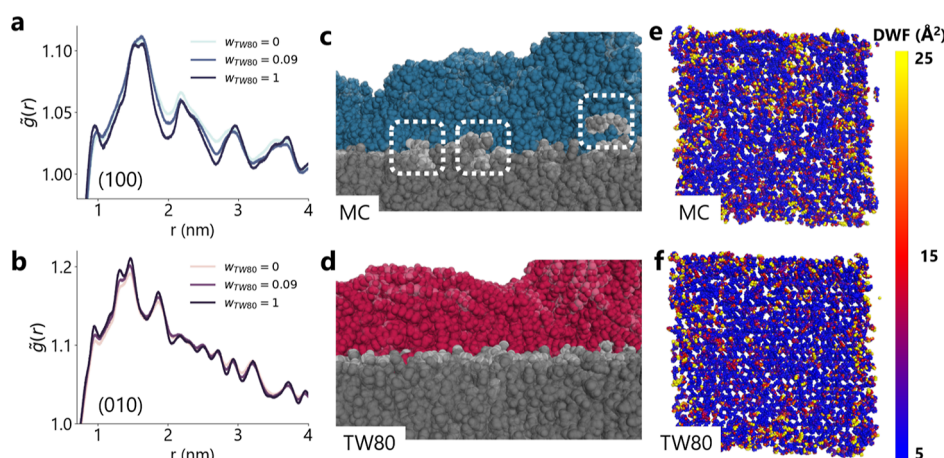

Figure 2. Polymer destructures the drug surface, while surfactant preserves surface structure. Atomistic self-RDF for the (a) (100) and (b) (010) crystallographic faces, with series highlighting increasing surfactant weight fractions. Simulation box side view showing the destructuring of the crystal surface (gray) in the presence of polymer (blue) (c) and the preserved structure of the crystal surface in the presence of surfactant (red) (d). White boxes in (c) indicate highly amorphous regions. DWFs mapped to the crystal surfaces in the all-MC (e) and all-TW80 (f) compositions. DWFs are shown in Å².

4. RESULTS AND DISCUSSION

4.1. Excipients Control Drug Crystal Structure. Nanocrystalline thin films containing FEN nanocrystals were synthesized using our group's method for bottom-up nanocrystallization. First, drug-loaded nanoemulsions are synthesized, then immobilized in a gel matrix that is cast into a thin film.[11] The solvent is evaporated, crystallizing spheroidal drug nanocrystals in the polymer matrix (see Experimental Section). We use a model hydrophobic drug, FEN, which is an ideal candidate for nanoformulation.[4] In this process, nonionic surfactants (TW80 or SP80) are used to stabilize nanodroplets during emulsification, while a gelling polymer (MC) generates a hydrogel scaffold that separates droplets during evaporative crystallization. This approach is representative of bottom-up nanocrystal synthesis that uses macromolecular excipients, and these excipients were selected for their generally recognized as safe (GRAS) status[35] and their frequent use in pharmaceutical

formulations. In nanoformulations, nonionic surfactants like TW80 and SP80 are used to stabilize nanocrystal surfaces.[51] Cellulose-derivatives like MC are used in nanoformulations to control release, bind powders, and stabilize nanocrystal surfaces.[52]

A representative SEM micrograph of a thin film nanocomposite shows spheroidal FEN nanocrystals embedded throughout the MC matrix (Figure 1a). Importantly, the XRD scattering pattern in Figure 1b highlights how polymers and surfactants can control the crystallization outcome. Surfactant removal from the formulation lowers the XRD intensity substantially due to decreased FEN crystallinity.[53] The extent of a drug's crystallinity plays an important role in its dissolution, stability, and processability.[54,55] Additionally, the crystallization-inhibiting ability of cellulosic polymers (including MC) is well-reported.[17,52,56] Experiments focused on preventing crystallization in ASDs have also identified that nonionic surfactants like TW80 can promote crystallization,
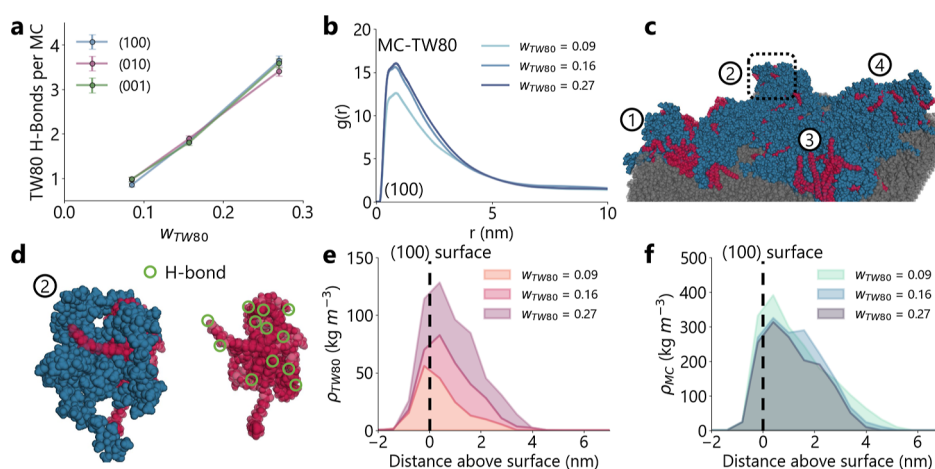
Figure 3. Polymer and surfactant exhibit complexation. (a) Average number of hydrogen bonds between TW80 and MC per MC molecule as a function of the surfactant weight fraction, w_{TW80} (wt %). Error bars indicate one standard deviation. Series indicate different crystallographic faces. (b) Atomistic RDF between MC and TW80 atoms in the simulations of the (100) crystal face at different surfactant weight fractions. (c) Molecular visualization showing four exemplars of MC (blue)−TW80 (red) complexation above the crystal. (d) Expanded view of exemplar 2 in (c) showing (left) an MC−TW80 complex containing five TW80 molecules and six MC oligomers. (right) Visualization of the surfactants in the complex, with the hydrogen bond contacts between TW80 and MC, highlighted with green circles. Visualizations are from the simulation of the (010) crystallographic face with w_{TW80} = 0.16. (e) Density profiles of TW80, ρ_{TW80} (kg m^{-3}), as a function of distance above the crystal surface. (f) Density profiles of MC, ρ_{MC} (kg m^{-3}), as a function of distance above the crystal surface. Darker curves indicate higher surfactant weight fractions.

potentially due to the alignment of flexible hydrophobic tails, which act as nucleants.[57,58] However, the ability of surfactants to modulate the extent of crystallinity of pharmaceutical nanosolids during a bottom-up synthesis has not been reported. Since surfactants are used to control dissolution, nanocrystal size, or other formulation properties, isolating the effect of surfactants on crystallinity is important for formulation design. Therefore, we investigated this mechanism by simulating the interfacial self-assembly of MC and TW80 on FEN crystal surfaces as previously described and characterizing the resulting interfacial and crystal structures (Figure 1e).

Using MD simulations, we first analyzed the effects on the FEN crystal surface, where the atomistic self-RDF of the top layer of the (100) and (010) FEN surfaces monotonically sharpens as w_{TW80} is increased (Figure 2a,b), suggesting that the local structure of the crystal increases with increasing w_{TW80}. This phenomenon is visualized in Figure 2c,d, where we observe a more structured surface when w_{TW80} = 1 (all-TW80) compared to the amorphized surface when w_{TW80} = 0 (all-MC). When w_{TW80} = 0, distinct regions of surface amorphization emerge (highlighted in white boxes), including some FEN molecules which completely separated from the crystal. Atomistic DWFs mapped onto the crystal surfaces reveal islands of higher molecular flexibility when w_{TW80} = 0 than w_{TW80} = 1, which correspond to the more amorphized regions of the crystal surface (Figure 2e,f). These trends match expectations from the literature, wherein TW80 is a known crystallization enhancer,[57,58] while MC and other cellulose-derivatives are known crystallization inhibitors in pharmaceutical systems.[17,52,56] However, previous simulations studying drug crystal interactions with excipients have focused on energetics rather than structure due to limited time scales in simulations relative to the time scales of phase transitions.[29,30,59−61] Additionally, previous simulations also have not simulated experimentally relevant compositions of excipients, preventing analyses from exploring experimentally relevant effects on crystals. Here, we unlock the direct comparison to experiments by simulating realistic composi-

tions, allowing us to observe how excipients modify the drug crystal structure.

4.2. Polymer−Surfactant Complexation and Competitive Chemisorption Drive Interfacial Structure. After establishing the effect of TW80 and MC on the FEN crystal, we next characterized the intermolecular interactions between these macromolecular excipients, since these interactions determine the surface conditions and ultimately the net effect on the drug crystal structure. First, we observed and analyzed MC−TW80 complexation, driven by both van der Waals interactions and hydrogen bonding. Polymer−surfactant aggregation and complexation have been previously observed and characterized in many systems with polymers and surfactants,[58,62,63] but less work has explored this phenomenon in the presence of a solid interface on which both species adsorb.[64] Favorable MC−TW80 intermolecular interactions are expected, since both molecules are amphiphilic and have both hydrogen bond donor (2 per MC monomer, 3 per TW80) and acceptor (9 per MC monomer, 9 per TW80) sites. On all three crystallographic faces, the number of MC−TW80 H-bonds per MC increases monotonically with w_{TW80} (Figure 3a). The atomistic MC−TW80 RDF in Figure 3b exhibits a peak around 1 nm, characteristic of H-bonding. This structured MC−TW80 RDF is consistent across all three crystallographic faces (Figure S6, Supporting Information). Previously published MD simulations found similar synergistic interactions between a related cellulose derivative, hydroxypropyl MC, and TW80, but did not characterize H-bonding.[29] The MC−TW80 Lennard-Jones interaction energy ranges between −100 and 400 kJ/mol MC for all compositions, suggesting the polymer and surfactant have strongly stable nonbonded interactions (Figure S8, Supporting Information). This is intuitive, since the unsaturated hydrocarbon tail of TW80 and the methylated ethers in MC can form hydrophobic contacts due to the hydrophobic effect. We observe MC−TW80 complexation above the drug surface, where several distinct complexes emerge, roughly resembling surfactant core-polymer shell structures (Figure 3c,d). This core−shell H-
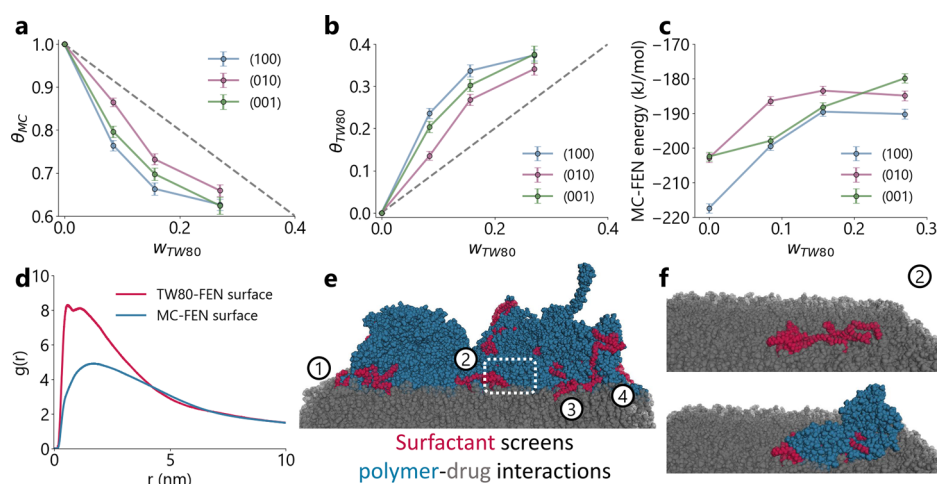
Figure 4. Surfactant screens polymer−surface interactions. Relative surface coverage of MC θ_{MC} (a) and TW80 θ_{TW80} (b) as a function of w_{TW80}. Dotted line shows parity. Error bars correspond to standard deviation in the relative surface coverage during the production run of the simulation. (c) Lennard-Jones short-range interaction energy between MC and the crystal surface as a function of w_{TW80}. Error bars correspond to standard deviation in the energy during the production run of the simulation. (a−c) Series represent the three different crystallographic faces simulated ((100), (010), and (001)). (d) Atomistic RDF between MC and the FEN surface (blue) and TW80 and the FEN surface (red). (e) Molecular visualization showing four exemplars of the surfactant (red) "screening" the polymer (blue) from the crystal surface. (f) Expanded view of exemplar 2 in (e) showing only the surfactant and drug (top) and all three components (bottom). Visualizations are from the simulation of the (100) crystallographic face with $w_{TW80} = 0.09$.

bond complex is analogous to the hydrophobic microenvironment of a folded protein, which can facilitate internal H-bonding.[65] The z-density profiles of TW80 and MC (Figure 3e,f) show component density parallel to the surface, exhibiting a primary peak on the crystal surface (∼0 nm). However, as w_{TW80} increases, we observe that both MC and TW80 develop a secondary density peak ∼1.5 nm above the crystal surface due to the formation of MC−TW80 complexes in the excipient layer. Importantly, the complexation between MC and polysorbate-type surfactants was previously hypothesized based on experimental results but never confirmed.[66,67]

We next characterized the interactions of the excipients with the drug crystal surface, where we observed competitive interfacial chemisorption between MC and TW80. We first define the relative surface coverage, θ for both excipients, as shown in eqs 8 and 9 below

$$\theta_{MC} = \frac{\langle H_{MC} \rangle}{\langle H_{MC} \rangle + \langle H_{TW80} \rangle} \tag{8}$$

$$\theta_{TW80} = \frac{\langle H_{TW80} \rangle}{\langle H_{MC} \rangle + \langle H_{TW80} \rangle} \tag{9}$$

where θ_{MC} is the surface coverage of MC, θ_{TW80} is the surface coverage of TW80, $\langle H_{MC} \rangle$ is the time-averaged number of H-bonds between MC and the crystal surface, and $\langle H_{TW80} \rangle$ is the time-averaged number of H-bonds between TW80 and the crystal surface. As w_{TW80} increases, θ_{MC} decreases nonlinearly below unity (Figure 4a), while θ_{TW80} correspondingly increases nonlinearly above unity (Figure 4b) for all three crystal surfaces. This suggests preferential H-bonding between the surfactant and crystal surface, at the expense of polymer-crystal H-bonding. This surfactant "screening" effect is further observed through the MC−FEN interaction energy, where the strong MC−FEN interaction is destabilized by the addition of surfactant (Figure 4c). We can structurally observe this preferential adsorption in the atomistic RDFs of each excipient relative to the (100) drug surface, where a sharp peak at $r \approx$

0.5 nm corresponds to strongly chemisorbed TW80 molecules (Figure 4d). This sharp peak characteristic of strong TW80 chemisorption is also visible on the (010) and (001) faces (Figure S6, Supporting Information). Several exemplars of this screening are highlighted in Figure 4e. The tight chemisorption of TW80 prevents MC from interacting with the surface, which may explain why an increasing surfactant weight fraction can preserve crystal structure (Figure 4f). Surfactant preferentially localizes to the surface and prevents MC interfacial adsorption, which is known to lead to inhibited crystal growth via lattice breakup.[68] Since both MC and TW80 are tensioactive, the outcome of this competitive surface adsorption is nontrivial. To our knowledge, this is the first molecular analysis of such competitive surface adsorption on drug crystal surfaces.

These coupled phenomena of MC−TW80 complexation and TW80 screening support a mechanism previously proposed in the context of oil-in-water emulsions. Gullapalli and Sheth probed the effects of MC and polysorbate-type surfactants on emulsion stability, hypothesizing that polysorbate would first preferentially adsorb, then MC would adsorb and complex to the polysorbate layer, finally followed by MC penetration to the oil/water interface depending on the polysorbate surface coverage.[66] Complexation and screening/multilayer adsorption can together explain related experimental results in colloidal and emulsion stability, ASD design, and crystal growth.[24,58,64,69] Our simulations support these previous experimental results, characterizing cellulose-polysorbate complexation and polysorbate screening and contextualizing the implications of these phenomena in dictating interfacial structure in colloidal and nanoparticle surfaces.

4.3. Bulk Crystal Dynamics Reveal Mechanism of Amorphization. After revealing the mechanisms of MC−surfactant complexation and surfactant screening, we characterized how these mechanisms influence drug crystal structure, particularly the extent of crystallinity. We also compare how these mechanisms generalize to systems using another surfactant, SP80. Nanocrystalline thin films were synthesized
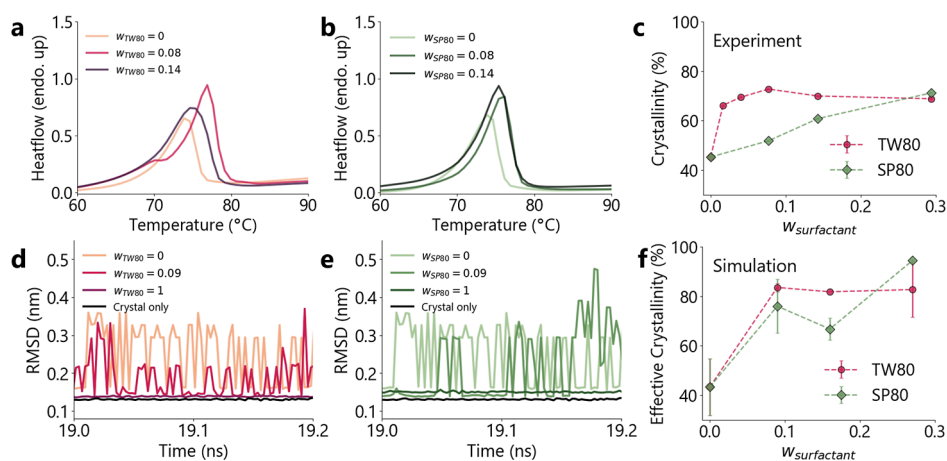
Figure 5. Bulk crystal dynamics correlate to experimental crystallinity. Background-subtracted DSC thermograms of nanocrystalline thin films using varying amounts of (a) TW80 and (b) SP80 surfactant. Darker curves correspond to increasing surfactant weight fraction. (c) Calculated extent of crystallinity as a function of surfactant weight fraction for TW80 (red) and SP80 (green) surfactants. rmsd (nm) against time (ns) of the middle layer of the (100) crystal relative to the crystal lattice structure for simulations with (d) TW80 as the surfactant and (e) SP80 as the surfactant. Darker curves correspond to increasing surfactant weight fraction. (f) Simulated effective crystallinity using eq 10 as a function of $w_{surfactant}$ for simulations with TW80 (red) and SP80 (green), averaged across all three crystallographic faces. Error bars correspond to the standard deviation in the effective crystallinity across the three crystallographic faces.

with $w_{surfactant}$ parametrically varied between 0 and 0.29 for both TW80 and SP80 (Table S2, Supporting Information Section). After performing bottom-up crystallization, the melting point behavior was characterized using DSC for formulations using TW80 (Figure 5a) and SP80 (Figure 5b) as the surfactant. The extent of crystallinity was calculated for each formulation using the measured thermograms as described previously, yielding the curves in Figure 5c. With TW80, the crystallinity of the FEN nanoparticles increases sharply at low $w_{surfactant}$, then plateaus. In contrast, with SP80, the crystallinity increases roughly linearly with $w_{surfactant}$. These crystallinity trends are stable over 2 months, with storage at room temperature and pressure (Figure S11, Supporting Information).

Since a crystallinity metric is difficult to define in molecular simulations,[70] we draw an analogy in our simulations using the fluctuations observed in the crystal far from the surface. While the time scale of crystal amorphization may be inaccessible to molecular simulations, we reasoned that short-time (ns) structural fluctuations and deviations from the crystal lattice positions may correlate to the macroscopic amorphization behavior. We thus define an effective crystallinity for a given crystallographic face ($\Gamma_{effective,i}$) from our simulations using eq 10 below

$$\Gamma_{effective} = \frac{\frac{a}{2} - \langle rmsd \rangle}{\frac{a}{2} - \langle rmsd_0 \rangle} \tag{10}$$

where $\langle rmsd_0 \rangle$ is the time average of the rmsd of the middle layer of the crystal in the absence of excipients, $\langle rmsd \rangle$ is the time average of the rmsd of the middle layer of the crystal in a given simulation, and a is the lattice spacing between unit cells along the a crystallographic axis (0.81605 nm). Here, $rmsd_0$ and rmsd are computed as deviations from the atomic positions of the lattice. This approach normalizes the measured deviation to the minimum thermal deviation of the crystal in the absence of excipients, while the maximum deviation is set to $\frac{a}{2}$. For both surfactants, we observe that the crystal deviations decrease as $w_{surfactant}$ increases, with the deviation

in the $w_{surfactant} = 1$ simulation approaching the thermal minimum for both surfactants (Figure 5d,e). However, when we transform these fluctuations to effective crystallinity using eq 10 and average across the three crystallographic surfaces, we observe similar trends to the experimentally observed crystallinity (Figure 5f). The effective FEN crystallinity in the TW80 simulations quickly increases and plateaus at higher $w_{surfacant}$ compositions, while the effective crystallinity increases roughly linearly in the SP80 simulations.

The different crystallinity trends of FEN in TW80 and SP80 formulations shed light on the dominant intermolecular mechanism that controls the FEN crystallinity. These surfactants have different hydrophilic−lipophilic balances (HLB), where $HLB_{TW80} = 15$ and $HLB_{SP80} = 4.3$. We expect that the more lipophilic SP80 should have stronger preferential surface adsorption than the more hydrophilic TW80. Indeed, θ_{SP80} deviates further from unity than θ_{TW80} (Figure S12, Supporting Information). However, we find that SP80 is less effective than TW80 at forming H-bonds with MC oligomers, likely since SP80 has only 6 hydrogen bond acceptors, while TW80 has 9 (Figure S13, Supporting Information). Since drug crystallinity sharply increases with a small amount of TW80 but not with a small amount of SP80, surfactant−polymer complexation resulting in polymer delocalization from the surface is likely the driving mechanism that explains surfactant-dependent crystallinity in drug nanoparticles. This is, to our knowledge, the first direct comparison between experimental and simulated extents of crystallinity and the first report of quantitative trends in the extent of crystallinity as a function of excipient composition. We find that the trends of effective crystallinity defined in our simulations qualitatively agree with the experimentally measured crystallinity. The extent of crystallinity is an important metric for drug product performance, but it is notoriously difficult to predict and rationalize a priori.[55] Here, we revealed how excipient composition controls destabilization in drug crystals, which could be the short-time scale precursors to bulk amorphization. Understanding these molecular drivers of crystallinity is crucial to unlocking the

rational design of enabling formulations with desired product profiles and physical properties.

5. CONCLUSIONS

Overall, this work explores how excipient composition influences drug nanocrystal solid state structure. We experimentally observe the surfactant-dependent extent of crystallinity in FEN nanocrystals templated from nanodroplets and use MD simulations to reveal the intermolecular phenomena that drive the crystallization outcome. In single-excipient simulations, we observe how MC destructures the crystal surfaces, while TW80 surfactants can preserve crystallinity. In mixtures of MC and surfactant, we observe and characterize complexation driven by H-bonding and hydrophobic/van der Waals interactions, which were previously hypothesized in related experimental results. We also observe and characterize surfactant screening, where surfactant molecules preferentially surface adsorb and protect the drug surface from MC interactions. Finally, we draw an analogy to the extent of crystallinity in our simulations using short time-scale fluctuations in atomic positions, finding qualitative agreement in the crystallinity between experiments and simulations. Our simulations reveal how different excipients can control drug crystallinity, which is particularly important in the design of enabling formulations, which leverage excipients to control drug structure to improve dissolution. This study demonstrates how molecular simulation can reveal fundamental molecular interactions and powerfully inform formulation design.

■ ASSOCIATED CONTENT

Data Availability Statement

GitHub repository with supporting code and input files for MD simulations in GROMACS: https://github.com/lucasattia/drug-surface-MD.

Ⓢ Supporting Information

The Supporting Information is available free of charge at https://pubs.acs.org/doi/10.1021/acsami.4c06815.

> Derivation of excipient composition, formatting crystal slabs, oligomer model design, validation of restraints on crystal, excipient insertion strategy, equilibration of simulations, hydrogen bonding and interaction energy results, analysis of crystal structure, comparison of TW80 and SP80 hydrogen bonding and interaction energy, and design of nanoemulsion-based thin films, materials, experimental characterization, and simulation reproducibility and robustness (PDF)

■ AUTHOR INFORMATION

Corresponding Author

Patrick S. Doyle − *Department of Chemical Engineering, Massachusetts Institute of Technology, Cambridge, Massachusetts 02139, United States; Campus for Research Excellence and Technological Enterprise, Singapore 138602, Singapore;* ⓞ orcid.org/0000-0003-2147-9172; Email: pdoyle@mit.edu

Authors

Lucas Attia − *Department of Chemical Engineering, Massachusetts Institute of Technology, Cambridge, Massachusetts 02139, United States;* ⓞ orcid.org/0000-0002-9941-3846

Dien Nguyen − *Department of Chemical Engineering, Massachusetts Institute of Technology, Cambridge, Massachusetts 02139, United States;* ⓞ orcid.org/0009-0000-9229-4154

Devashish Gokhale − *Department of Chemical Engineering, Massachusetts Institute of Technology, Cambridge, Massachusetts 02139, United States;* ⓞ orcid.org/0000-0003-2545-2735

Talia Zheng − *Department of Chemical Engineering, Massachusetts Institute of Technology, Cambridge, Massachusetts 02139, United States;* ⓞ orcid.org/0009-0006-0814-1344

Complete contact information is available at:
https://pubs.acs.org/10.1021/acsami.4c06815

Notes

The authors declare no competing financial interest.

■ REFERENCES

(1) Porter, C. J. H.; Trevaskis, N. L.; Charman, W. N. Lipids and lipid-based formulations: optimizing the oral delivery of lipophilic drugs. *Nat. Rev. Drug Discovery* **2007**, *6*, 231−248.

(2) Singh, A.; Worku, Z. A.; Van den Mooter, G. Oral formulation strategies to improve solubility of poorly water-soluble drugs. *Expet Opin. Drug Deliv.* **2011**, *8*, 1361−1378.

(3) Rabinow, B. E. Nanosuspensions in drug delivery. *Nat. Rev. Drug Discovery* **2004**, *3*, 785−796.

(4) Kawabata, Y.; Wada, K.; Nakatani, M.; Yamada, S.; Onoue, S. Formulation design for poorly water-soluble drugs based on biopharmaceutics classification system: basic approaches and practical applications. *Int. J. Pharm.* **2011**, *420*, 1−10.

(5) Liversidge, G. G.; Cundy, K. C. Particle size reduction for improvement of oral bioavailability of hydrophobic drugs: I. Absolute oral bioavailability of nanocrystalline danazol in beagle dogs. *Int. J. Pharm.* **1995**, *125*, 91−97.

(6) Hammond, R. B.; Pencheva, K.; Roberts, K. J.; Auffret, T. Quantifying solubility enhancement due to particle size reduction and crystal habit modification: case study of acetyl salicylic acid. *J. Pharm. Sci.* **2007**, *96*, 1967−1973.

(7) Schenck, L.; Erdemir, D.; Saunders Gorka, L.; Merritt, J. M.; Marziano, I.; Ho, R.; Lee, M.; Bullard, J.; Boukerche, M.; Ferguson, S.; Florence, A. J.; Khan, S. A.; Sun, C. C. Recent Advances in Co-processed APIs and Proposals for Enabling Commercialization of These Transformative Technologies. *Mol. Pharmaceutics* **2020**, *17*, 2232−2244.

(8) Johnson, B. K.; Prud'homme, R. K. Flash NanoPrecipitation of Organic Actives and Block Copolymers using a Confined Impinging Jets Mixer. *Aust. J. Chem.* **2003**, *56*, 1021−1024.

(9) Saad, W. S.; Prud'homme, R. K. Principles of nanoparticle formation by flash nanoprecipitation. *Nano Today* **2016**, *11*, 212−227.

(10) Attia, L.; Chen, L.-H.; Doyle, P. S. Orthogonal Gelations to Synthesize Core-Shell Hydrogels Loaded with Nanoemulsion-Templated Drug Nanoparticles for Versatile Oral Drug Delivery. *Adv. Healthcare Mater.* **2023**, *12*, No. e2301667.

(11) Chen, L.-H.; Doyle, P. S. Thermogelling Hydroxypropyl Methylcellulose Nanoemulsions as Templates to Formulate Poorly Water-Soluble Drugs into Oral Thin Films Containing Drug Nanoparticles. *Chem. Mater.* **2022**, *34*, 5194−5205.

(12) Chen, L.-H.; Doyle, P. S. Design and Use of a Thermogelling Methylcellulose Nanoemulsion to Formulate Nanocrystalline Oral Dosage Forms. *Adv. Mater.* **2021**, *33*, No. e2008618.

(13) Domenech, T.; Doyle, P. S. High Loading Capacity Nanoencapsulation and Release of Hydrophobic Drug Nanocrystals from Microgel Particles. *Chem. Mater.* **2020**, *32*, 498−509.

(14) Badruddoza, A. Z. M.; Godfrin, P. D.; Myerson, A. S.; Trout, B. L.; Doyle, P. S. Core-shell composite hydrogels for controlled nanocrystal formation and release of hydrophobic active pharmaceutical ingredients. *Adv. Healthcare Mater.* **2016**, *5*, 1960−1968.

(15) Eral, H. B.; O'Mahony, M.; Shaw, R.; Trout, B. L.; Myerson, A. S.; Doyle, P. S. Composite Hydrogels Laden with Crystalline Active Pharmaceutical Ingredients of Controlled Size and Loading. *Chem. Mater.* **2014**, *26*, 6213−6220.

(16) Vasconcelos, T.; Sarmento, B.; Costa, P. Solid dispersions as strategy to improve oral bioavailability of poor water soluble drugs. *Drug Discovery Today* **2007**, *12*, 1068−1075.

(17) Chavan, R. B.; Rathi, S.; Jyothi, V. G. S. S.; Shastri, N. R. Cellulose based polymers in development of amorphous solid dispersions. *Asian J. Pharm. Sci.* **2019**, *14*, 248−264.

(18) Zhang, H.; Wang, D.; Butler, R.; Campbell, N. L.; Long, J.; Tan, B.; Duncalf, D. J.; Foster, A. J.; Hopkinson, A.; Taylor, D.; Angus, D.; Cooper, A. I.; Rannard, S. P. Formation and enhanced biocidal activity of water-dispersable organic nanoparticles. *Nat. Nanotechnol.* **2008**, *3*, 506−511.

(19) Raghavan, S. L.; Trividic, A.; Davis, A. F.; Hadgraft, J. Crystallization of hydrocortisone acetate: influence of polymers. *Int. J. Pharm.* **2001**, *212*, 213−221.

(20) Ilevbare, G. A.; Liu, H.; Edgar, K. J.; Taylor, L. S. Impact of polymers on crystal growth rate of structurally diverse compounds from aqueous solution. *Mol. Pharmaceutics* **2013**, *10*, 2381−2393.

(21) Poornachary, S. K.; Chia, V. D.; Yani, Y.; Han, G.; Chow, P. S.; Tan, R. B. H. Anisotropic Crystal Growth Inhibition by Polymeric Additives: Impact on Modulation of Naproxen Crystal Shape and Size. *Cryst. Growth Des.* **2017**, *17*, 4844−4854.

(22) He, S.; Kan, A. T.; Tomson, M. B. In *Water Soluble Polymers: Solutions Properties and Applications*; Amjad, Z., Ed.; Springer US: Boston, MA, 2002; pp 163−171.

(23) Ye, X.; Wang, Z.; Zhang, J.; Wan, X. Noncovalently functionalized commodity polymers as tailor-made additives for stereoselective crystallization. *Angew. Chem., Int. Ed.* **2021**, *60*, 20243.

(24) Ilevbare, G. A.; Liu, H.; Edgar, K. J.; Taylor, L. S. Effect of Binary Additive Combinations on Solution Crystal Growth of the Poorly Water-Soluble Drug, Ritonavir. *Cryst. Growth Des.* **2012**, *12*, 6050−6060.

(25) Indulkar, A. S.; Gao, Y.; Raina, S. A.; Zhang, G. G. Z.; Taylor, L. S. Impact of Monomeric versus Micellar Surfactant and Surfactant−Polymer Interactions on Nucleation−Induction Times of Atazanavir from Supersaturated Solutions. *Cryst. Growth Des.* **2020**, *20*, 62−72.

(26) Prasad, D.; Chauhan, H.; Atef, E. Role of Molecular Interactions for Synergistic Precipitation Inhibition of Poorly Soluble Drug in Supersaturated Drug-Polymer-Polymer Ternary Solution. *Mol. Pharmaceutics* **2016**, *13*, 756−765.

(27) Zidan, A. S.; Rahman, Z.; Sayeed, V.; Raw, A.; Yu, L.; Khan, M. A. Crystallinity evaluation of tacrolimus solid dispersions by chemometric analysis. *Int. J. Pharm.* **2012**, *423*, 341−350.

(28) Rawlinson, C. F.; Williams, A. C.; Timmins, P.; Grimsey, I. Polymer-mediated disruption of drug crystallinity. *Int. J. Pharm.* **2007**, *336*, 42−48.

(29) Zhu, W.; Romanski, F. S.; Meng, X.; Mitra, S.; Tomassone, M. S. Atomistic simulation study of surfactant and polymer interactions on the surface of a fenofibrate crystal. *Eur. J. Pharm. Sci.* **2011**, *42*, 452−461.

(30) Zhu, W.; Romanski, F. S.; Dalvi, S. V.; Dave, R. N.; Silvina Tomassone, M. Atomistic simulations of aqueous griseofulvin crystals in the presence of individual and multiple additives. *Chem. Eng. Sci.* **2012**, *73*, 218−230.

(31) Gupta, K. M.; Yani, Y.; Poornachary, S. K.; Chow, P. S. Atomistic Simulation To Understand Anisotropic Growth Behavior of Naproxen Crystal in the Presence of Polymeric Additives. *Cryst. Growth Des.* **2019**, *19*, 3768−3776.

(32) Yani, Y.; Chow, P. S.; Tan, R. B. H. Molecular simulation study of the effect of various additives on salbutamol sulfate crystal habit. *Mol. Pharmaceutics* **2011**, *8*, 1910−1918.

(33) Ndlovu, S. T.; Ullah, N.; Khan, S.; Ramharack, P.; Soliman, M.; de Matas, M.; Shahid, M.; Sohail, M.; Imran, M.; Shah, S. W. A.; Hussain, Z. Domperidone nanocrystals with boosted oral bioavailability: fabrication, evaluation and molecular insight into the polymer-domperidone nanocrystal interaction. *Drug Delivery Transl. Res.* **2019**, *9*, 284−297.

(34) Edueng, K.; Mahlin, D.; Larsson, P.; Bergström, C. A. Mechanism-based selection of stabilization strategy for amorphous formulations: Insights into crystallization pathways. *J. Controlled Release* **2017**, *256*, 193−202.

(35) FDA SCOGS (Select Committee on GRAS Substances). https://www.cfsanappsexternal.fda.gov/scripts/fdcc/?set=SCOGS (accessed Oct 20, 2022).

(36) Malde, A. K.; Zuo, L.; Breeze, M.; Stroet, M.; Poger, D.; Nair, P. C.; Oostenbrink, C.; Mark, A. E. An Automated Force Field Topology Builder (ATB) and Repository: Version 1.0. *J. Chem. Theory Comput.* **2011**, *7*, 4026−4037.

(37) Hanwell, M. D.; Curtis, D. E.; Lonie, D. C.; Vandermeersch, T.; Zurek, E.; Hutchison, G. R. Avogadro: an advanced semantic chemical editor, visualization, and analysis platform. *J. Cheminf.* **2012**, *4*, 17.

(38) Jha, P. K.; Larson, R. G. Assessing the efficiency of polymeric excipients by atomistic molecular dynamics simulations. *Mol. Pharmaceutics* **2014**, *11*, 1676−1686.

(39) Zoete, V.; Cuendet, M. A.; Grosdidier, A.; Michielin, O. SwissParam: a fast force field generation tool for small organic molecules. *J. Comput. Chem.* **2011**, *32*, 2359−2368.

(40) Vanommeslaeghe, K.; Hatcher, E.; Acharya, C.; Kundu, S.; Zhong, S.; Shim, J.; Darian, E.; Guvench, O.; Lopes, P.; Vorobyov, I.; Mackerell, A. D. CHARMM general force field: A force field for drug-like molecules compatible with the CHARMM all-atom additive biological force fields. *J. Comput. Chem.* **2010**, *31*, 671−690.

(41) Giannos, T.; Lešnik, S.; Bren, U.; Hodošček, M.; Domratcheva, T.; Bondar, A.-N. CHARMM Force-Field Parameters for Morphine, Heroin, and Oliceridine, and Conformational Dynamics of Opioid Drugs. *J. Chem. Inf. Model.* **2021**, *61*, 3964−3977.

(42) Rukmani, S. J.; Kupgan, G.; Anstine, D. M.; Colina, C. M. A molecular dynamics study of water-soluble polymers: analysis of force fields from atomistic simulations. *Mol. Simul.* **2019**, *45*, 310−321.

(43) Mosquera-Giraldo, L. I.; Borca, C. H.; Meng, X.; Edgar, K. J.; Slipchenko, L. V.; Taylor, L. S. Mechanistic Design of Chemically Diverse Polymers with Applications in Oral Drug Delivery. *Biomacromolecules* **2016**, *17*, 3659−3671.

(44) Henry, R. F.; Zhang, G. Z.; Gao, Y.; Buckner, I. S. Fenofibrate. *Acta Crystallogr., Sect. E: Struct. Rep. Online* **2003**, *59*, o699−o700.

(45) Macrae, C. F.; Sovago, I.; Cottrell, S. J.; Galek, P. T. A.; McCabe, P.; Pidcock, E.; Platings, M.; Shields, G. P.; Stevens, J. S.; Towler, M.; Wood, P. A. Mercury 4.0: from visualization to analysis, design and prediction. *J. Appl. Crystallogr.* **2020**, *53*, 226−235.

(46) Van Der Spoel, D.; Lindahl, E.; Hess, B.; Groenhof, G.; Mark, A. E.; Berendsen, H. J. C. GROMACS: fast, flexible, and free. *J. Comput. Chem.* **2005**, *26*, 1701−1718.

(47) Bussi, G.; Donadio, D.; Parrinello, M. Canonical sampling through velocity rescaling. *J. Chem. Phys.* **2007**, *126*, 014101.

(48) Flensburg, C.; Stewart, R. F. Lattice dynamical Debye-Waller factor for silicon. *Phys. Rev. B: Condens. Matter Mater. Phys.* **1999**, *60*, 284–291.

(49) Ridgway, M. C.; Glover, C. J.; Azevedo, G. d. M.; Kluth, S. M.; Yu, K. M.; Foran, G. J. Structure in amorphous semiconductors: Extrinsic and intrinsic. *Nucl. Instrum. Methods Phys. Res., Sect. B* **2005**, *238*, 294–301.

(50) Dwyer, L. M.; Michaelis, V. K.; O'Mahony, M.; Griffin, R. G.; Myerson, A. S. Confined crystallization of fenofibrate in nanoporous silica. *CrystEngComm* **2015**, *17*, 7922–7929.

(51) Peltonen, L.; Hirvonen, J. Pharmaceutical nanocrystals by nanomilling: critical process parameters, particle fracturing and stabilization methods. *J. Pharm. Pharmacol.* **2010**, *62*, 1569–1579.

(52) Sievens-Figueroa, L.; Bhakay, A.; Jerez-Rozo, J. I.; Pandya, N.; Romañach, R. J.; Michniak-Kohn, B.; Iqbal, Z.; Bilgili, E.; Davé, R. N. Preparation and characterization of hydroxypropyl methyl cellulose films containing stable BCS Class II drug nanoparticles for pharmaceutical applications. *Int. J. Pharm.* **2012**, *423*, 496–508.

(53) Rumondor, A. C. F.; Taylor, L. S. Application of partial least-squares (PLS) modeling in quantifying drug crystallinity in amorphous solid dispersions. *Int. J. Pharm.* **2010**, *398*, 155–160.

(54) Gao, D.; Rytting, J. H. Use of solution calorimetry to determine the extent of crystallinity of drugs and excipients. *Int. J. Pharm.* **1997**, *151*, 183–192.

(55) Moseson, D. E.; Taylor, L. S. Crystallinity: A Complex Critical Quality Attribute of Amorphous Solid Dispersions. *Mol. Pharmaceutics* **2023**, *20*, 4802–4825.

(56) Mosquera-Giraldo, L. I.; Borca, C. H.; Parker, A. S.; Dong, Y.; Edgar, K. J.; Beaudoin, S. P.; Slipchenko, L. V.; Taylor, L. S. Crystallization Inhibition Properties of Cellulose Esters and Ethers for a Group of Chemically Diverse Drugs: Experimental and Computational Insight. *Biomacromolecules* **2018**, *19*, 4593–4606.

(57) Chen, J.; Ormes, J. D.; Higgins, J. D.; Taylor, L. S. Impact of surfactants on the crystallization of aqueous suspensions of celecoxib amorphous solid dispersion spray dried particles. *Mol. Pharmaceutics* **2015**, *12*, 533–541.

(58) Deshpande, T. M.; Shi, H.; Pietryka, J.; Hoag, S. W.; Medek, A. Investigation of Polymer/Surfactant Interactions and Their Impact on Itraconazole Solubility and Precipitation Kinetics for Developing Spray-Dried Amorphous Solid Dispersions. *Mol. Pharmaceutics* **2018**, *15*, 962–974.

(59) Heng, W.; Song, Y.; Luo, M.; Hu, E.; Wei, Y.; Gao, Y.; Pang, Z.; Zhang, J.; Qian, S. Mechanistic insights into the crystallization of coamorphous drug systems. *J. Controlled Release* **2023**, *354*, 489–502.

(60) Gao, Y.; Olsen, K. W. Drug-polymer interactions at water-crystal interfaces and implications for crystallization inhibition: molecular dynamics simulations of amphiphilic block copolymer interactions with tolazamide crystals. *J. Pharm. Sci.* **2015**, *104*, 2132–2141.

(61) Gao, Y.; Olsen, K. W. Drug-polymer interactions at water-crystal interfaces and implications for crystallization inhibition: molecular dynamics simulations of amphiphilic block copolymer interactions with tolazamide crystals. *J. Pharm. Sci.* **2015**, *104*, 2132–2141.

(62) Kłos, J. S.; Paturej, J. Complexation between Dendritic Polyelectrolytes and Amphiphilic Surfactants: The Impact of Surfactant Concentration and Hydrophobicity. *Macromolecules* **2023**, *56*, 5022–5032.

(63) Saito, S. Solubilization properties of polymer-surfactant complexes. *J. Colloid Interface Sci.* **1967**, *24*, 227–234.

(64) Kronberg, B.; Kuortti, J.; Stenius, P. Competitive and cooperative adsorption of polymers and surfactants on kaolinite surfaces. *Colloids Surf.* **1986**, *18*, 411–425.

(65) Creighton, T. E. *Proteins: Structures and Molecular Properties*; Macmillan, 1993.

(66) Gullapalli, R. P.; Sheth, B. B. Effect of methylcellulose on the stability of oil-in-water emulsions. *Int. J. Pharm.* **1996**, *140*, 97–109.

(67) Gullapalli, R. P.; Sheth, B. B. Effect of methylcellulose on the stability of oil-in-water emulsions: influence of the disperse phase. *Int. J. Pharm.* **1997**, *151*, 249–253.

(68) Wang, Y.; Xue, F.; Yu, S.; Cheng, Y.; Yin, M.; Du, S.; Gong, J. Insight into the morphology and crystal growth of DL-methionine in aqueous solution with presence of cellulose polymers. *J. Mol. Liq.* **2021**, *343*, 116967.

(69) Sarker, D. K.; Axelos, M.; Popineau, Y. Methylcellulose-induced stability changes in protein-based emulsions. *Colloids Surf., B* **1999**, *12*, 147–160.

(70) Cordina, R. J.; Smith, B.; Tuttle, T. Rapid Automated Quantification of Triacylglyceride Crystallinity in Molecular Dynamics Simulations. *J. Chem. Inf. Model.* **2022**, *62*, 5601–5606.